IEEE Robotics and Automation Letters (RA-L) paper, presented at ICRA 2026, Vienna, Austria. Cite as RA-L paper.

Non-Rigid Motion Compensation With Skin Deformation Prediction for in Situ Bioprinting

Lénaïc Cuau, Philippe Poignet, and Nabil Zemiti

***Abstract*—This letter introduces a novel method of non-rigid motion compensation for in situ bioprinting. Most bioprinting platforms use open-loop systems, but it raises concerns about patient safety and suboptimal wound coverage in case of patient motion. To handle these issues, our method integrates an RGB-D camera to manage orientation and to predict deformations, along with a laser telemeter to regulate deposited material thickness. The proposed approach has been evaluated on a moving silicone platform that deforms at 0.8 Hz with a 4 mm in-plane amplitude and a 20 mm elevation amplitude. Our method resulted in a wound coverage error of less than 1%. Comparative analysis demonstrates a 73.0% enhancement in deforming path following compared to existing methods. Additionally, by predicting surface motion, the method enables more precise control of layer height, with an error inferior to 0.1mm.**

***Index Terms*—In situ bioprinting, non-rigid motion compensation, visual servoing, medical robots and systems.**

I. Introduction

THE treatment of extensive burns presents a challenge in reconstructive surgery, particularly for people burned at more than 50% where the conventional autologous skin grafting is unfeasible. In such cases, *in vitro* culture of skin substitutes is often employed, but has some limitations as prolonged treatment duration, graft manipulation complexities, inadequate wound coverage and the formation of unsightly scars. In situ bioprinting has emerged as a promising alternative since its introduction in 2010 as it enables direct deposition of skin cells onto the wound bed and addresses deep tissue burns [1], [2]. Given a 3D scan of the wound site, a printing trajectory can be established to fill the wound with a biomaterial [1] as a classical 3D-printer. Then, a robotic arm follows this path and precisely deposits the cells through a nozzle. Studies have shown that this approach improves both the speed and quality of wound healing compared to conventional methods [1].

However, even if this kind of platform has shown promising results, a critical gap exists in the literature concerning the compensation of patient motion during robotic bioprinting, particularly in abdominal regions. Respiratory movements introduce significant non-rigid spatial displacements in the range of 10 mm in antero-posterior direction and 3 mm in cranio-caudal direction [3], posing challenges to both procedural fidelity and collision risks with patient. To achieve optimal wound coverage, several factors are important, including: respecting edges, guaranteeing constant layer thickness and avoiding collisions. This can be ensured by controlling three parameters: tool-to-surface distance, tool orientation, and tool position. However, only a few works have tried to address this issue and none have simultaneously accounted for all three parameters to compensate for non-rigid motion. Initial attempts were done for compensating rigid only motion. O'Neill et al. [4] employed a 3 DOF system equipped with a LeapMotion camera to infer hand movements. But this method is constrained by its localized applicability to the hand. Zhao et al. [5] endeavored to use a 6 DOF platform to compensate for rigid displacements and orientation changes through contour detection methodologies, necessitating uninterrupted contour visibility throughout the bioprinting process. Fortunato et al. [6] explored QR code-based compensation techniques, but were limited to rectify rigid displacements such as Chaudry et al. [7] who employed a marker-based visual control loop. However, the true motion of breathing is not rigid as the skin can expand and contract [3]. Zhu et al. [8] and Smith et al [9] considered this factor in their work by using markers positions to compute the surface deformation. However, the use of such markers is not feasible in the considered application due to limited healthy areas for placement, and increased infection risk. On their side, Kucukdeger et al. [10] proposed to use a laser telemeter for guaranteeing precise deposit by servoing the distance from the nozzle to the surface. While allowing a constant thickness of deposit, this process does not allow for filling a complete wound that is deforming since the laser does not provide information on 3D deformation. Finally, Barjuei et al. [11] proposed to use a vision system to adjust the robot path in order to maintain consistent filament spacing, but not in real time. In addition, in all the previously cited methods except [5], the tool orientation is not controlled making it difficult to attain challenging location and to completely fill complex surfaces. In conclusion, any method proposed in these works is compatible nor applicable to motion compensation during in situ bioprinting. To address these challenges, we propose a novel methodology integrating RGB-D camera technology and a laser telemeter to compensate for non-rigid skin motion while managing tool orientation. This approach represents an innovative solution that,

Received 22 January 2025; accepted 16 May 2025. Date of publication 30 May 2025; date of current version 9 June 2025. This letter was recommended for publication by Associate Editor A. Schlaefer and Editor J. Burgner-Kahrs upon evaluation of the reviewers' comments. This work was supported in part by French Project under Grant ANR-21-ASM2-0001 - Blocprint2, in part by the French Ministry of Defence - Defence Innovation Agency, and in part by the Region Occitanie - "Défi-clé Robotique centrée sur l'humain" *(Corresponding author: Lénaïc Cuau.)*

The authors are with the LIRMM CNRS, University of Montpellier, 34000 Montpellier, France (e-mail: lenaic.cuau@lirmm.fr).

This article has supplementary downloadable material available at https://doi.org/10.1109/LRA.2025.3575234, provided by the authors.

Digital Object Identifier 10.1109/LRA.2025.3575234

IEEE Robotics and Automation Letters (RA-L) paper, presented at ICRA 2026, Vienna, Austria. Cite as RA-L paper.

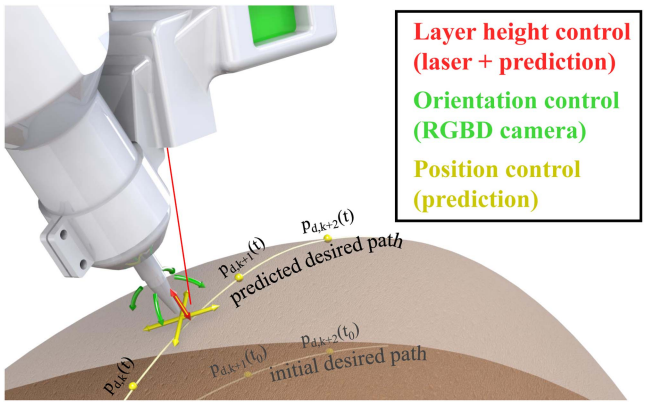

Fig. 1. Overview of the proposed non-rigid motion compensation method.

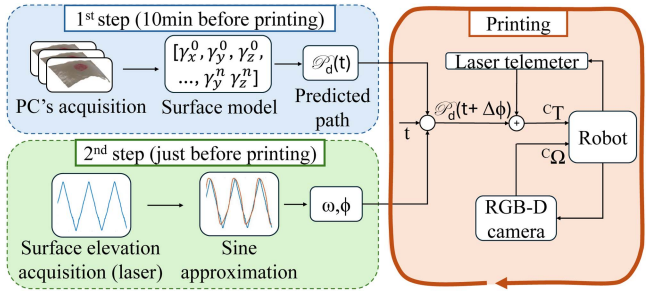

Fig. 2. A summary of the proposed robot control method workflow.

for the first time to the authors knowledge, simultaneously controls for all three critical parameters: tool-to-surface distance, tool orientation, and tool position (Fig. 1).

In our work, we employ an RGB-D camera to perform offline estimation and prediction of expansion and retraction of the skin, treating it as a Thin Plate Spline (TPS) surface model. Additionaly, we integrate two sensors to provide real-time feedback for enhanced safety and precision. Firstly, a laser telemeter is utilized to ensure precise control over layer height. Secondly, the same RGB-D camera is employed to maintain the robot's orientation normal to the surface

The letter is organized as follows: in Section II, the used method is detailed from the printing path prediction to the robot control. Then, in Section III, the method is evaluated on a silicone platform which is deforming. Finally, the results are exposed and discussed in Section IV.

II. Methodology

A. Method Overview

Let's consider a printing trajectory based on the RGB-D scan of the wound. This path is denoted as $\mathscr{P}(t_0) = \{\mathbf{p}_1(t_0), \mathbf{p}_2(t_0), \ldots, \mathbf{p}_N(t_0)\}$ where N is a strictly positive integer that represents the number of reference points, and $\mathbf{p}_k(t_0) \in \mathbb{R}^3$ are the desired tool positions at initial time t_0 when the path was defined. Due to the dynamic nature of the considered surface, it becomes necessary to continually update this trajectory throughout the task. Assuming a burned patient is mechanically ventilated during surgery, the temporal deformation of the trajectory is learned offline. The surface deformation is first recorded during enough periods of time using the RGB-D camera and the deformed trajectory $\mathscr{P}(t)$ is predicted using a Kalman Filter (KF) (Section II-C1). This prediction is finally integrated into the robot control for precise trajectory tracking, compensating for non-rigid motion (Section II-C). Additionaly, a laser telemeter is introduced to regulate layer height (Section II-C2), while the RGB-D camera serves to adjust the nozzle orientation relative to the surface (Section II-B). An overview of the entire process is depicted in Fig. 2. In this section, first the orientation control with visual servoing (VS) is presented. Then, the position control is described through the surface motion prediction and the feedback loop control of the layer height.

B. Orientation Control

The objective is to align the nozzle axis with the surface normal using visual servoing. To maintain the nozzle's perpendicularity to the surface, as recommended in [12], we use an embedded RGB-D camera in an eye-in-hand configuration. This setup allows for online estimation of the surface normal. The camera is rigidly mounted on the robot. It captures both the end effector and the surface, eliminating errors due to the robot's kinematic model and bypassing the need for a known kinematic relationship between the robot and the camera.

The kinematic relationship between the camera C and the nozzle tip P can be defined as

$$ {}^{C}\mathbf{T}_P = \begin{bmatrix} | & | & | & | \\ {}^{C}\mathbf{x}_P & {}^{C}\mathbf{y}_P & {}^{C}\mathbf{z}_P & {}^{C}\mathbf{t}_P \\ | & | & | & | \\ 0 & 0 & 0 & 1 \end{bmatrix} \tag{1} $$

with ${}^{C}\mathbf{x}_P$,${}^{C}\mathbf{y}_P$,${}^{C}\mathbf{z}_P$ the axis associated with the nozzle expressed in C, and ${}^{C}\mathbf{t}_P$ the translation vector from camera to nozzle tip. To determine those vectors, the nozzle is placed on a given point perpendicularly to a flat surface with three ArUco markers engraved on it. Through marker detection in the image (${}^{C}\mathbf{T}_M$), and knowing perfectly by Computer Aided Design (CAD) the nozzle's position relative to the markers (${}^{M}\mathbf{t}_P$), we can determine $\begin{bmatrix} {}^{C}\mathbf{t}_P \\ 1 \end{bmatrix} = {}^{C}\mathbf{T}_M \begin{bmatrix} {}^{M}\mathbf{t}_P \\ 1 \end{bmatrix}$. As the nozzle's axis $\mathbf{z}_P$ is placed perpendicular to the surface, it can be computed by analyzing the observed Point Cloud (PC) and getting surface normal. While ${}^{C}\mathbf{x}_P$ and ${}^{C}\mathbf{y}_P$ can be defined arbitrarily, we choose ${}^{C}\mathbf{y}_P = [0\ 1\ 0]$, and compute ${}^{C}\mathbf{x}_P$ as the cross product of ${}^{C}\mathbf{y}_P$ and ${}^{C}\mathbf{z}_P$ (Fig. 3).

During printing, the normal to the surface of interest should be established in front of the nozzle at $\mathbf{p} = {}^{C}\mathbf{t}_P + [\delta_x, 0, 0]^T$ where δ_x is the nozzle radius. To do so, the acquired PC is cropped within a semi-spherical region of radius 15mm (based on surface curvature) centered on the nozzle tip. As previously indicated, a laser telemeter is used for layer height correction. To avoid interferences with this laser, data points within a 5 mm radius sphere centered around the nozzle tip are excluded from the PC. On the remaining PC, a plane is estimated using a RANSAC method and its normal ${}^{C}\mathbf{n}$ is computed (Fig. 3). Given the inherent noise in the PC, a KF is employed to mitigate variations

IEEE Robotics and Automation Letters (RA-L) paper, presented at ICRA 2026, Vienna, Austria. Cite as RA-L paper.

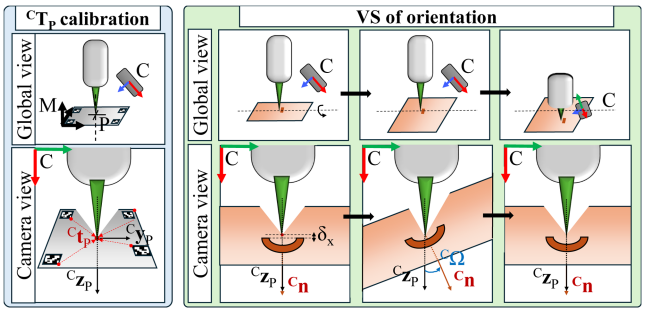

Fig. 3. Complete method to perform orientation control. The blue part represent the estimation of ${}^C\mathbf{T}_P$ by placing the nozzle perpendicular to a flat surface. The green part is the workflow of the VS method : initially ${}^C\mathbf{n}$ (computed in the red semi-circle) and ${}^C\mathbf{z}_P$ (from calibration) are aligned. When surface moves ${}^C\mathbf{\Omega}$ is computed with eq.2 to align ${}^C\mathbf{z}_P$ with ${}^C\mathbf{n}$ resulting, in the global view, in the robot aligned with surface normal.

and anticipate occlusions or failures. The state vector is defined as $E_n = [{}^C n_x, {}^C n_y, {}^C n_z, {}^C \dot{n}_x, {}^C \dot{n}_y, {}^C \dot{n}_z]^T$, and adjustments to measurement and prediction noise are tailored to the characteristics of the employed camera system. To align the nozzle axis with surface normal, the angular velocity in the camera's frame is computed as

$$ {}^C\mathbf{\Omega} = K_o {}^C\mathbf{z}_P \wedge {}^C\mathbf{n} \tag{2}$$

with K_o a scalar gain. In the robot base frame B, it gives

$$ {}^B\mathbf{\Omega} = {}^B\mathbf{R}_C . {}^C\mathbf{\Omega} \tag{3}$$

with ${}^B\mathbf{R}_C = {}^B\mathbf{R}_P ({}^C\mathbf{R}_P)^{-1}$ the rotation matrix between the robot base frame and the camera's frame obtained through robot kinematic model and prior tool calibration. It is important to highlight that with this formulation, alignment of the axes persists even in the presence of calibration or robot kinematic errors, as ${}^C\mathbf{\Omega}$ becomes null if and only if the axes are aligned in the camera's frame.

C. Position Control

As the previous orientation control ensures that the robot remains consistently perpendicular to the deforming surface, we now focus on the robot's motion along the surface, aiming to follow the predicted path while maintaining a constant layer height.

1) Motion Prediction: In the context of severe burn injuries, patients are typically sedated and mechanically ventilated, resulting in a respiratory motion pattern that is considered perfectly periodic. Consequently, acquiring knowledge of this periodicity prior to printing enables effective compensation strategies to be implemented.

As explained in [13], the deformation of a surface can be modelised as a Thin Plate Spline (TPS) warp $w_{3D} : \mathbb{R}^3 \to \mathbb{R}^3$, which maps each point $\mathbf{p} \in \mathbb{R}^3$ in a given PC to its corresponding coordinates $\mathbf{p}' \in \mathbb{R}^3$ in the deformed PC. This mapping is determined by the coordinates of the TPS Control Points (TPS-CP) $\mathbf{c}'(t) = \begin{bmatrix}\mathbf{c}'_\mathbf{x}(\mathbf{t}) & \mathbf{c}'_y(t) & \mathbf{c}'_z(t)\end{bmatrix}^T$ where $\mathbf{c}'_x(t), \mathbf{c}'_y(t)$ and $\mathbf{c}'_z(t)$ represent respectively the vector of x, y and z coordinates of each TPS-CP at time t. In other words, $\forall \mathbf{p} \in \mathbb{R}^3$, the transformed point is given by $\mathbf{p}' = w_{3D}(\mathbf{p}, \mathbf{c}'(t))$. Therefore, to adjust the inital desired path to the current deformed surface, the coordinates of the TPS-CP over time $\mathbf{c}'(t)$ must be predicted.

As we consider a periodic motion, each coordinate of each TPS-CP can be modelised as a Fourier Serie as presented in [14]. That is to say, if we denote $\mathbf{c}'_i(t)$ the i-th line of $\mathbf{c}'(t)$ (which represents the i-th TPS-CP), we have $\mathbf{c}'_i(t) = [x'_i(t), y'_i(t), z'_i(t)] \in \mathbb{R}^3$ and we can write:

$$ x'_i(t) = a^i_{0,x} + \sum_{k=1}^{H} a^i_{k,x}\cos(\omega t) + b^i_{k,x}\sin(\omega t) \tag{4}$$

and similarly for $y'_i(t)$ and $z'_i(t)$. With H the chosen number of harmonics to modelise the movements and ω the motion frequency. The objective is to determine the Fourier Series coefficients $\{a_{k,x}, b_{k,x}, a_{k,y}, b_{k,y}, a_{k,z}, b_{k,z}\}_{k=0:H}$. To do so, the breathing motion is recorded as a sequence of 3D colored PCs during at least three periods. Each 3D TPS-CP are tracked in the sequence using color and depth informations as presented in [15], giving $\mathbf{c}'(t)$ for all $t \in [0, 3\frac{2\pi}{\omega}]$.

To iteratively estimate the Fourier coefficients based on the found TPS-CP at each time step, a KF is used. The vector of parameters is defined as $E = [\gamma^0_x, \gamma^0_y, \gamma^0_z, \ldots, \gamma^n_x, \gamma^n_y, \gamma^n_z]$, where n represents the number of TPS-CP and $\gamma^i_X = [a^i_{0,X}, \ldots, a^i_{H,X}, b^i_{0,X}, \ldots, b^i_{H,X}]$ the parameters of point i (with $X = x$ or y or z). The frequency ω is computed afterwards with laser acquisition. So the Kalman Filter can be written as:

$$ \begin{cases} \mathbf{E}(t) = \mathbf{E}(t-1) + \mathbf{Q} \\ \mathbf{c}'(t) = \mathbf{C}(t)\mathbf{E}(t) + \mathbf{R} \end{cases} \tag{5}$$

with $\mathbf{C}(t) = \begin{bmatrix}1 & \cos(\omega t) & \cos(2\omega t) & \ldots & \sin(H\omega t)\end{bmatrix}$, and $\mathbf{Q}$, $\mathbf{R}$ the process and measurement error covariance matrices respectively. In our case, diagonal values of $\mathbf{Q}$ and $\mathbf{R}$ are set all equal to 1, as model and measures are both uncertain, and we do not have more *a priori* knowledge. Utilizing classical linear KF algorithm, the Fourier coefficient are estimated, enabling estimation of the TPS-CP $\mathbf{c}'(t)$ at each time t. These estimated TPS-CP are then utilized to predict the deformed trajectory using $\mathscr{P}(t) = w_{3D}(\mathscr{P}(t_0), \mathbf{c}'(t))$.

Due to computational constraints, the tracking of $\mathbf{c}'(t)$ in each PC of the sequence and estimation of Fourier coefficients is performed offline some minutes before application. Then, prior to printing, the prediction needs to be synchronized with the actual patient motion (Fig. 2). To achieve this alignment, the robotic arm is positioned anywhere above the surface equipped with a laser telemeter just before printing. Laser measurement of surface are then recorded for at least three periods. The resulting output is a sinusoidal signal given by $A\sin(\omega t + \phi)$, whose parameters (A, ω, ϕ) can be determined via least-square error minimization. The phase of the predicted signal can be analytically estimated as $\phi_k = \arctan(\frac{a^i_{1,z}}{b^i_{1,z}})$, where the point i is an arbitrary chosen point from the TPS-CP grid. The phase difference $\Delta\phi = \phi_k - \phi$ is then used to correct the predicted trajectory, yielding $\mathscr{P}(t) = w_{3D}(\mathscr{P}(t_0), \mathbf{c}'(t + \Delta\Phi))$.

To accurately track the moving trajectory $\mathscr{P}(t)$, the control along the nozzle axis is decoupled from the robot's motion

IEEE Robotics and Automation Letters (RA-L) paper, presented at ICRA 2026, Vienna, Austria. Cite as RA-L paper.

along the surface. This decoupling is essential for maintaining consistent robot progression at a constant velocity v. To achieve this, at each time step, the next desired robot position is defined as:

$$\mathbf{p}_d(t) = \mathbf{p}_d(t - dt) + \boldsymbol{\delta_p}(t) + \boldsymbol{\delta_z}(t) \tag{6}$$

where $\boldsymbol{\delta_z}$ represents the correction for layer height, while $\boldsymbol{\delta_p}$ accounts for the robot's travel along the surface at a constant velocity, independent of $\boldsymbol{\delta_z}$. Each term will be detailed in Section II-C2 and II-C3.

2) Layer Height Correction: By predicting the surface deformation as described in Section II-C1, we can determine analytically by derivating equations (4) the velocity of each control point $\mathbf{v}'_\mathbf{c}(t) = \frac{d\mathbf{c}'}{dt} = [\frac{d\mathbf{c}'_1(t)}{dt}, \ldots, \frac{d\mathbf{c}'_n(t)}{dt}]^T$. Consequently, the velocity of each point along the path $\mathscr{P}$ is derived as :

$$\forall k \in [1, N], \mathbf{v}_{\mathbf{p},k}(t) = w_{3D}(\mathbf{p}_k(t_0), \mathbf{v}'_\mathbf{c}(t + \Delta\Phi)) \tag{7}$$

The layer height correction is then managed using a PID controller, supplemented by a feed-forward term that accounts for the established speed in the nozzle direction :

$$\boldsymbol{\delta_z}(t) = (K_p(h(t) - l) + K_i \int (h(t) - l)dt + K_d \frac{d}{dt}(h(t) - l) + \langle \mathbf{v}_{\mathbf{p},k}(t)\ ,\ {}^B\mathbf{z}_P(t)\rangle){}^B\mathbf{z}_P(t)dt \tag{8}$$

with k the index of the next target point, K_p, K_i, K_d the scalar PID gains and $\langle ., . \rangle$ which defines the scalar product between two vectors. The constant l denotes the desired layer height, while $h(t)$ represents the measurement obtained from the laser telemeter.

3) Decoupled Trajectory Tracking: The decoupled component $\boldsymbol{\delta_p}$, representing the robot's progress along the surface at constant speed v is defined as :

$$\boldsymbol{\delta_p} = \overline{(\tilde{\mathbf{p}}_k(t) - \tilde{\mathbf{p}}_{k-1}(t))}vdt \tag{9}$$

where the operator $\overline{\mathbf{u}}$ defines the vector normalization, dt is the sampling time and $\tilde{\mathbf{p}}_k(t)$ is calculated using (10), where dependance on t remains but (t) notation is omitted for clarity:

$$\tilde{\mathbf{p}}_k = \mathbf{p}_k + \delta_\alpha \underline{{}^B\mathbf{z}_P} + \langle(\mathbf{p}_k + \delta_\alpha - \tilde{\mathbf{p}}_{k-1}), {}^B\mathbf{z}_P \wedge \mathbf{z}\rangle\mathbf{z} \tag{10}$$

with $\delta_\alpha = hcos(\alpha)$. This defines $\tilde{\mathbf{p}}_k$ as the point belonging to the line (d_a) perpendicular to the current nozzle axis $({}^B\mathbf{z}_P)$ passing through the robot's previous position $(\tilde{\mathbf{p}}_{k-1})$. This ensures that the robot motion along the path is independent of any corrections made by the laser sensor. Besides, $\tilde{\mathbf{p}}_k$ is constrained to lie on the vertical line (d_b) passing through $\mathbf{p}_k + \delta_\alpha \underline{{}^B\mathbf{z}_P}$, with $\underline{{}^B\mathbf{z}_P} = [{}^B\mathbf{z}_{P,x}, {}^B\mathbf{z}_{P,y}, 0]^T$. This adjustment accounts for the fact that the material deposition point is offset from the nozzle tip of distance h measured by the laser sensor. k is incremented when $\|\mathbf{p}_d - \tilde{\mathbf{p}}_k\| > D_k$ with D_k the inital distance from $\mathbf{p}_d$ to $\tilde{\mathbf{p}}_k$ (Fig. 4). This enables the robot to advance at a constant velocity v in the direction parallel to the surface while the layer height is corrected in the direction perpendicular to the surface. We thus obtain the cartesian velocity control law:

$$\begin{cases} {}^B\boldsymbol{\Omega} = {}^B\mathbf{R}_C.{}^C\boldsymbol{\Omega} \\ {}^B\mathbf{T} = K(\mathbf{p}_d(t) - {}^B\mathbf{t}_P) \end{cases} \tag{11}$$

with $K \in \mathbb{R}$. The algorithm is detailed in Algorithm 1.

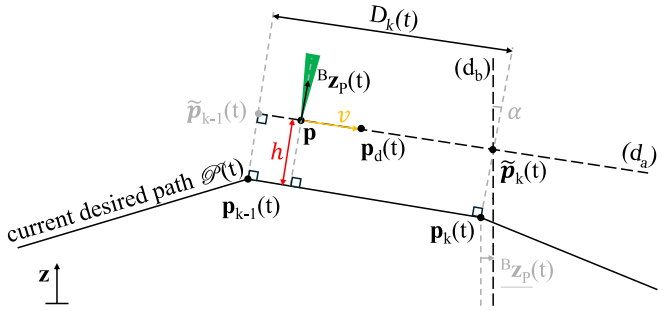

Fig. 4. The robot trajectory is controlled in the nozzle axis direction based on the telemeter and in the perpendicular plane by the predicted path pose.

Algorithm 1: Cartesian Velocity Control Loop of the Robot.

$k \leftarrow 0$; $t \leftarrow 0$;
$\mathbf{p}_d \leftarrow \mathscr{P}(t)[k]$; $\mathbf{p}_{start} \leftarrow \mathbf{p}_d$; $\mathbf{p}_{end} \leftarrow \mathscr{P}(t)[k+1]$
while $k < N$ **do**
  Get deformed path $\mathscr{P}(t)$, nozzle orientation ${}^B\mathbf{z}_P$, laser distance h, surface normal ${}^C\mathbf{n}$
  $\boldsymbol{\delta_z} \leftarrow PID(h - l)$
  $\tilde{\mathbf{p}}_k \leftarrow$
  $\mathbf{p}_{end} + \delta_\alpha \underline{{}^B\mathbf{z}_P} + \langle(\mathbf{p}_{end} + \delta_\alpha - \mathbf{p}_{start}), {}^B\mathbf{z}_P \wedge \mathbf{z}\rangle\mathbf{z}$
  $\boldsymbol{\delta_p} \leftarrow \overline{(\tilde{\mathbf{p}}_k - \mathbf{p}_{start})}vdt$
  $\mathbf{p}_d \leftarrow \mathbf{p}_d + \boldsymbol{\delta_z} + \boldsymbol{\delta_p}$
  $D_k \leftarrow \|\tilde{\mathbf{p}}_k - \mathbf{p}_{start}\|$
  if $\|\mathbf{p}_d - \mathbf{p}_{start}\| > D_k$ **then**
    $k \leftarrow k + 1$
    $\mathbf{p}_{start} \leftarrow \mathbf{p}_d$
    $\mathbf{p}_{end} \leftarrow \mathscr{P}_d(t)[k+1]$
  end if
  ${}^B\mathbf{T} \leftarrow K(\mathbf{p}_{start} - \mathbf{p})$
  ${}^B\boldsymbol{\Omega} \leftarrow {}^B R_C(K_o {}^C\mathbf{z}_P \wedge {}^C\mathbf{n})$
  $t \leftarrow t + dt$
end while

III. Experiments and Results

The present section assesses the proposed method using four criteria: (1) the accuracy of the proposed orientation control and its effects on printing, (2) the accuracy when following a simple path on a deformable surface, (3) the comparison of wound coverage between our approach and the state-of-the-art method [10], and (4) the distance error from the surface during printing. The used robotic arm is a Panda (Franka Emika). The RGB-D camera is an IntelRealSense D405 (Intel). It uses a stereoscopic system to compute depth map and its range is 7–50 cm. The distance sensor is an Acuity AR100-50 whose range goes from 30 to 80 mm with an accuracy of 5 μm at 55 mm. The print-head is a ViproHead-3 (ViscoTec Pumpen).

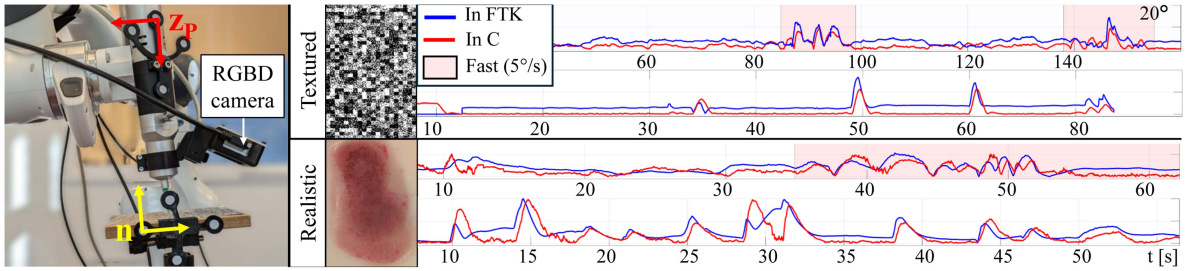

Fig. 5. The setup and results of orientation tracking (first and third row) and response to impulse (second and fourth row) on textured and realistic surface.

TABLE I
EXPERIMENTAL PARAMETERS FOR ORIENTATION CONTROL

Description	Parameter(s)	Value
Measure point offset	δ_x	1 mm
Measure noise	r	10 (textured) / 1 (realistic)
Model noise	q	1
P gain eq.(2)	K_o	2 (textured) / 1 (realistic)
Loop time step	dt	20 ms

TABLE II
EXPERIMENTAL RESULTS FOR ORIENTATION CONTROL

	Resp. time (s)	Slow err. (°)	Fast err. (°)
Realistic Textured			
In C	1.8	1.4 ± 0.8	2.5 ± 2.3
In FTK	1.8	3.1 ± 1.4	4.1 ± 2.6
Realistic			
In C	3.1	2.4 ± 1.4	3.5 ± 2.7
In FTK	3.1	3.5 ± 1.8	4.6 ± 2.3

The proposed algorithm was implemented in C++ and was ran with an IntelCorei7-6820HQ CPU @ 2.70GHz.

A. Visual Servoing of Orientation

1) Performance Evaluation: First, the accuracy of the proposed orientation control method is evaluated by aligning the robot in real time with a tilting plane. Infrared markers are attached to the print-head and the tilting plane as depicted in Fig. 5, and detected with the FusionTrack500 (Atracsys) (FTK). The rotational error is defined as the angle between the plane normal $\mathbf{n}$ and the nozzle axis $\mathbf{z}_P$. Two kinds of surfaces are used: a highly textured surface (to evaluate the method in the best case) and a more realistic surface representing a burn wound (Fig. 5). During the experiments, the plane is manually moved slowly (approx. 2°/s), rapidly (approx. °5/s) and by impulsion (approx. 10°). The parameters used are given in Table I. The measurement noise covariance matrix diagonal values (all equal to r) were experimentally adjusted to find the good tradeoff between damping and stability. As the respiratory motion dynamics is slow (approx. 2mm/s) more importance was given to stability so r was set to 20 and model noise q to 1. The resulting errors are shown in Fig. 5 and summarized in Table II. Mean error between the plane normal and the nozzle axis is $3.4 \pm 1.9°$ on a textured platform and $4.0 \pm 2.1°$ on a reaslitic platform.

2) Printing on a Complex Surface: Secondly, we evaluate the method by printing PluronicF-68 on a realistic wound with varying curvature. The surface is a silicone replica from [16] (Fig. 6). Three orientation control strategies are compared: (1) a fixed vertical tool (used in 79% of 24 reviewed platforms [1]), (2) planning-based orientation [12], and (3) the proposed real-time estimation method. Each method is carried out three times. The printing results and angular deviations of the robot tool from the z-axis are shown in Fig. 6, with a focus on a curved region of the wound. Both planning-based and proposed vision-based methods show similar orientation variations, with an average angular difference of $5.4 \pm 4.5°$. Alternating peaks are more pronounced in the VS approach, likely due to inaccuracies in the RGB-D acquisition for normal estimation in the planning-based method, particularly in texture-poor regions. This hypothesis is supported by angular deviation analysis from the 3D mesh from [16]. Both methods allow precise alignment with the actual geometry with mean errors of $4.5 \pm 3.1°$, and $6.3 \pm 4.7°$ for planning and VS method respectively. The former is attributed to scan inaccuracies, while the latter is explained by delays (see Section III-A1). Given those small angular differences, their impact on printing performance is not statistically significant. The average covered areas are 21.4 ± 0.9 cm^2, 21.7 ± 0.3 cm^2, and 21.6 ± 0.5 cm^2 for the vertical, planning-based, and proposed methods respectively (Fig. 6). These results demonstrate that the proposed method performs comparably to state-of-the-art techniques even in presence of realistic wound curvature.

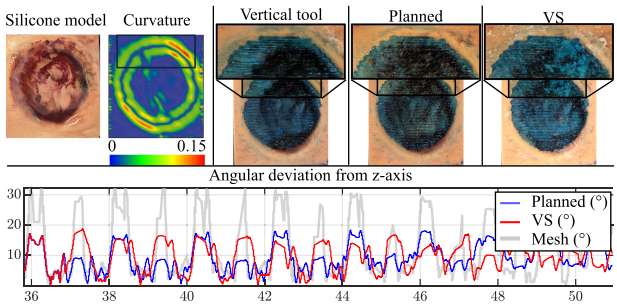

Fig. 6. On the left: pictures of the considered wound and its curvature in mm^{-1}. On the right : printing results for the three considered methods with a zoom in a curved area. Bottom row shows the angular deviation from z-axis for planning-based and VS method along with this deviation computed on the initial 3D mesh of the wound in the framed section.

3) Printing on an Inflated Surface: In this study, we evaluate the effect of orientation servoing when printing a line on a surface that undergoes deformation. The surface was made in Ecoflex50 and behaves as a balloon, undergoing non-rigid deformations through controlled inflation using a 200 ml syringe

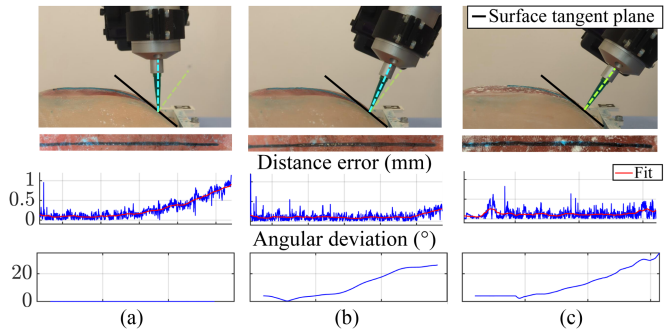

Fig. 7. Each column from left to right represents: (a) vertically oriented tool, (b) planning-based orientation, and (c) online normal estimation. The first row shows a photograph of the robot's orientation at the end of the line, the second row displays the printed line, the third row depicts the distance error from the desired layer height compared to laser measurements, and the last row illustrates the angular deviation from the vertical axis in degrees.

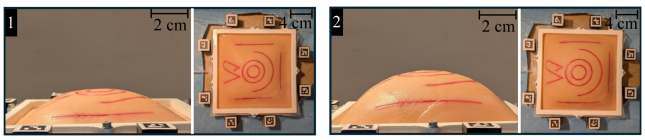

Fig. 8. Part 1 : Side view (left) and top view (right) of the used silicone platform when deflated. Part 2 : Side view (left) and top view (right) of the used silicone platform when inflated.

operated by a stepper motor. It can deform at a rate of 0.8 Hz with a 4 mm in-plane amplitude and a 20 mm elevation amplitude. The printed material is PluronicF-68. We consider the same three orientation control methods exposed in Section III-A2. The planned positions and orientations are computed on a completely deflated surface, and printing is done on a static inflated model. To assess the method performances, we compare the quality of the printed line, the distance error from the desired layer height, and the tool orientation (Fig. 7). Our observations reveal that surface orientation changes has occurred at the border of the deformed region due to breathing motion. The planned angular deviation from z-axis is almost linear from 0 to 26.3° while the real deviation, when surface is inflated, reaches 38.2°. Distance error increases in the presence of alignment errors as it can be seen at the end of the line (Fig. 7) where its value is 0.91 mm for scenario (1), 0.31 mm for scenario (2) and 0.21 mm for scenario (3). As expected (see Section III-A2), the impact of these orientation adjustments is not discernible in the continuity of the printed line, which remains consistent across all tested scenarios (Fig. 7).

B. Printing a Simple Path on Deforming Surface

In this section, we assess the accuracy of deformation tracking. We consider a silicone deformable surface made in Ecoflex50 with an arc and a circle engraved on it (Fig. 8). The goal is to follow those curves which undergo periodic deformations controlled with a syringe as explained in Section III-A3. The deformation parameters are the same as those given in Section III-A3. For fair comparison between printing results,

TABLE III
EXPERIMENTAL PARAMETERS

Description	Parameter(s)	Value
Harmonics	H	3
Gain eq.(2)	K_o	1.0
Gain eq.(11)	K	4.0
PID gains eq.(8)	$[K_p, K_i, K_d]$	[8.0, 10.0, 2.2]
Desired layer height	l	0.8 mm
Robot progress speed	v	3.0 mm/s
Loop time step	dt	20 ms

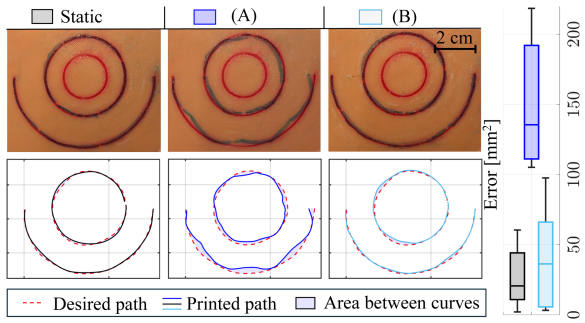

Fig. 9. On the left: printing results (top row) and extracted lines (bottom row). On the right: boxplot of the area between desired and printed path (N=5). (A) represents the method proposed in [10] and (B) our proposed method.

ArUco markers are placed around the platform (Fig. 8) to express the task and compare the results in a fixed reference frame. First, the printing path is manually defined in the robot base frame on an RGB-D scan of the surface. Then, during printing, the robot follows this pre-determined path while compensating for the surface's non-rigid motion using two different approaches that we will note Method (A) and Method (B). Method (A) is the compensation of tool-skin distance solely based on the laser feedback, as described in [10] with planned position and orientation. Method (B) is our proposed approach detailed in Section II. To establish a baseline for comparison, the desired path is also printed on the static shapes with method (A). Five prints are done for each method. The control parameters are set as given in the Table III. The gain values are determined experimentally to achieve an optimal balance between system stability and responsiveness. Three harmonics were selected ($H = 3$), as this number was experimentally determined as sufficient to approximate the triangular shape of elevation and in-plane deformation. The desired layer thickness was set to $l = 0.8$ mm, matching the nozzle diameter commonly used in bioprinting. The forward speed v was chosen to enhance material adhesion while ensuring a short printing time. The algorithm time step, dt, was set to the maximum computation time required for computing the deformed path. To compare the printed path and the desired path, pictures of the scene are done after each printing session. Each picture is registered and scaled thanks to the ArUco markers placed around the platform (Fig. 8). Then, the printed and desired path are manually detected and compared by computing the area between the two lines. The results, illustrated in Fig. 9, demonstrate that the desired trajectory is more accurately followed using our proposed method. The mean area between curves is 151.4 ± 45.9 mm^2 for method

IEEE Robotics and Automation Letters (RA-L) paper, presented at ICRA 2026, Vienna, Austria. Cite as RA-L paper.

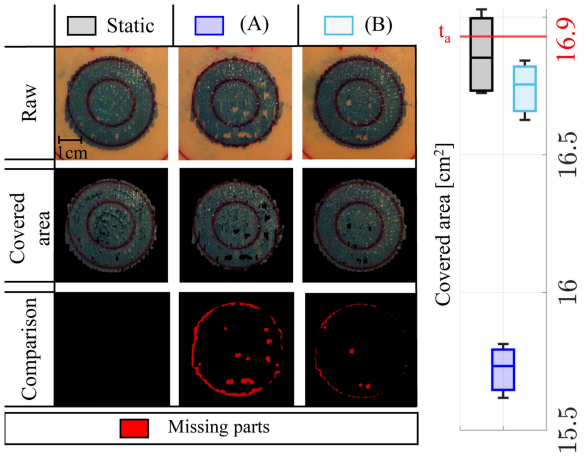

Fig. 10. On the left: the first row represents a photograph of the printing results, the second row is the extracted covered area, and the third row enhances the missing parts when printing with methods (A) or (B). (A) represents the method proposed in [10] and (B) our proposed method. On the right: a boxplot of the covered areas with each methods (N=3).

(A) and 40.5 ± 32.1 mm^2 for method (B) which represents a reduction of 73.2% of the error. The theoretical lower bound is 0 mm^2, however, in reality, due to misalignments or possible calibration errors, we can define practical lower bound as the area value when printing in static. Experimentally it is evaluated at 25.0 ± 20.1 mm^2. Thus, method (B) is 88% closer to practical lower bound than method (A).

C. Complete Wound Coverage for in Situ Bioprinting

To assess the efficacy of our approach for in situ bioprinting, a meaningful performance metric is wound coverage. The fundamental goal of in situ bioprinting is to achieve complete coverage of the wound with an uniformly distributed biomaterial. To quantify this, a covering pattern is defined on the previous surface with the method described in [17] to fill the bigger circle. As in previous section, the desired path is printed on the static platform (to establish a ground truth), and on the deforming platform with method (A), and with method (B). Each method was performed three times. The resulting printed material is automatically detected in the images in the HSV color space. Results are shown in Fig. 10. The results show that non-rigid compensation is essential to well attain the border of the wound and it results in a better wound coverage close to the best theoretical area (t_a) of 16.9cm^2 (when all the surface is covered). On average, less than 1% is not well covered with method (B) versus 6.5% with method (A) which represents 1.1cm^2 in our case. Regarding the distance from the surface, the error between the desired layer height and the measured distance over 300 seconds is shown in Fig. 11, along with surface elevation. The results demonstrate that the feed-forward term improves layer height control, achieving a mean distance error of 0.08 ± 0.05mm (max 0.35mm), compared to 0.11 ± 0.12mm (max 0.54mm) using a PID control alone. These values are within the intrinsic repeatability of the robot of 0.1mm.

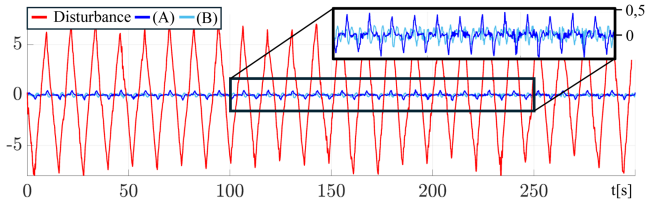

Fig. 11. Disturbance and distance error observed with methods (A) and (B) during complete wound coverage in mm.

IV. Discussion

The proposed approach allows for controlling orientation, position and layer height during in situ bioprinting enabling effective compensation of the surface deformations.

In the literature, most of the existing bioprinting platforms do not control the orientation of printing nozzle relative to the surface [1]. However it has been shown in [12], that aligning with surface normal is important, as it reduces collision risk, improve layer height control and allows to attain challenging locations. In the state-of-the-art, this is typically achieved by performing a 3D scan of the wound and precomputing surface normals offline, with which the nozzle aligns with during printing [12]. Nevertheless, registration or scanning error can occur and respiratory motion can alter these normals as shown in Fig. 7. Therefore, it is important to estimate and compensate for surface orientation in real-time during printing. One study has proposed using wound contour detection to estimate surface orientation [5], but this approach is limited by incomplete visibility of contours during printing, and approximates the wound as a rigidly moving plane. Moreover, as we have shown in Fig. 7 the surface orientation changes is more complex during deformation. To address this issue, we introduced a method based on an RGB-D camera in an eye-in-hand configuration, which allows for real-time detection of surface orientation at the nozzle tip. It enables the nozzle to dynamically align with deforming surface normals with a maximum error of 5° (Fig. 5). This enables realistic wound filling with performance comparable to state-of-the-art approaches (Fig. 6) while remaining robust to registration or scanning errors and being adaptive. This adaptive behavior ensures optimal layer height control, and collision avoidance in case of deforming surface (Fig. 7). However, it has to be noted that the stereoscopic vision technology used requires sufficient surface texture to accurately assess normals which implies noise in a realistic low-textured scenario, resulting in a filtering delay (+1.3 s) and greater error (+1°) (Fig. 5). Nevertheless, this delay does not influence the deposition accuracy even in curved (0.15mm^{-1}) areas (Fig. 6).

In addition, our method compensates for expansion and retraction of the wound. In the state-of-the-art, only two studies have been done to compensate for these factors [8], [9] using markers stuck on the surface. Such markers can be difficult to place on great burn patient and the methods are constrained to visibility of at least three of them. On the contrary, our method allows for learning offline a surface deformation model without markers based on TPS. Under the hypothesis that burn people are

usually sedated and mechanically ventilated, the model is used during printing to predict the adapted shape of the desired path. This allows to follow a deforming path with 73.2% less error than without predicting the deformation (Fig. 9). Additionaly, our method allows for precise control of layer height using a laser distance sensor along with the motion prediction. Compared to the PID-only controller (method (A)) inspired by [10], our method achieves a smaller average deviation (0.05 mm vs. 0.12 mm) and reduces peak deviations (0.35 mm vs. 0.54 mm), corresponding to 68% and 44% of the desired height (0.8 mm), respectively (Fig. 11). These improvements enhance patient collision avoidance, material adhesion and wound coverage (error $< 1\%$), which are critical factors for healing. However, the prediction is limited in time as a small error on ω estimation leads to a large error between predicted and real position after a certain amount of time. On the presented experiments ω is estimated with an error of $\pm 0.002\ rad.s^{-1}$. This results in a median duration of 4 minutes during which the error remains below 0.8 mm. After this time, the robot should stop and the current phase and frequency should be re-estimated with a new laser acquisition.

The parameter settings in Table III are key for high-quality printing. First, the number of harmonics H directly affects predicted signal accuracy and the system's capacity to handle sudden changes. While fewer harmonics reduce precision, the printing process is not highly sensitive to this parameter, and minor variations ($H = 2$ to 5) are acceptable. Gain selection is, for its part, critical. It must account for the printing system, printing speed, and breathing rate to balance responsiveness and stability. As with most PID-controlled systems, this tuning process demands meticulous adjustments for optimal performance. Additionally, the desired nozzle-to-skin distance l directly affects material deposit. If the nozzle is too close, the ink can accumulate around the edges, leading to errors, especially if the laser telemeter misinterprets this accumulation as the desired surface. Conversely, if the nozzle is too far, material adhesion to the skin is compromised. The nozzle diameter helps tuning this parameter, and careful calibration is essential. Lower printing speeds reduce sensitivity to both gains setting and l as slower movements allow for more accurate deposition. However, reducing the speed extend printing time, which increase the risk of hypothermia, infection, and physical fatigue of the patient. Therefore, an optimal balance between printing speed and ease of tuning is necessary for practical application given that the chosen parameters allow for printing 16 cm^2 in 10 min.

The main drawback of the proposed method lies in its reliance on predictable periodic motion. In situations where unexpected motion occurs, collision avoidance is ensured through the utilization of a distance sensor. However, the printing quality may suffer. Besides, after too long time or when changes in ventilator parameters occur, the system should pause and wait for the breathing parameters to stabilize, then learn the new parameters and resume printing. While this approach ensures accuracy, it increases the total printing time. Thus, investigating an online estimation approach for breathing parameters would be a promising avenue.

V. Conclusion

This letter introduces a novel approach for in situ bioprinting, incorporating non-rigid motion compensation via an RGB-D camera and a distance sensor. Diverging from existing methods, our approach effectively addresses orientation, elevation, expansion, and retraction of the wound without the need for markers. Comparative analysis reveals the superiority of our method in promoting wound coverage over a state-of-the-art technique that solely compensates for layer height. The proposed approach could therefore serve as a basis for future in situ bioprinting platforms to enhance the care of burn patients. Key areas for improvement include the coarseness of surface normal estimation and the assumption of periodic surface motion without temporal variations. These aspects provide valuable directions for future research endeavors.

References

[1] W. Zhao, C. Hu, and T. Xu, "In vivo bioprinting:broadening the therapeutic horizon for tissue injuries," *Bioactive Materials*, vol. 25, pp. 201–222, 2023.

[2] R. Y. Cheng et al., "Handheld instrument for wound-conformal delivery of skin precursor sheets improves healing in full-thickness burns," *Biofabrication*, vol. 12, no. 2, 2020, Art. no. 0 25002.

[3] T. Wentz et al., "Accuracy of dynamic patient surface monitoring using a time-of-flight camera and B-spline modeling for respiratory motion characterization," *Phys. Med. Biol.*, vol. 57, no. 13, pp. 4175–4193, 2012.

[4] J. J. O'Neill, R. A. Johnson, R. L. Dockter, and T. M. Kowalewski, "3D bioprinting directly onto moving human anatomy," in *Proc. IEEE/RSJ Int. Conf. Intell. Robots Syst.*, 2017, pp. 934–940.

[5] W. Zhao et al., "Adaptive multi-degree-of-freedom in situ bioprinting robot for hair-follicle-inclusive skin repair: A preliminary study conducted in mice," *Bioeng. Transl. Med.*, vol. 7, 2022, Art. no. e10303.

[6] G. M. Fortunato, A. F. Bonatti, E. Batoni, R. Macaluso, G. Vozzi, and C. De Maria, "Motion compensation system for robotic based in situ bioprinting to balance patient physiological movements," *Bioprinting*, vol. 28, 2022, Art. no. e00248.

[7] M. S. Chaudhry and A. Czekanski, "Visual control for robotic 3D printing on a moving platform," *Mechatronics*, vol. 100, 2024, Art. no. 103191.

[8] Z. Zhu et al., "3D printed functional and biological materials on moving freeform surfaces," *Adv. Materials*, vol. 30, no. 23, 2018, Art. no. 1707495.

[9] R. Smith et al., "Towards robotic bioprinting directly onto moving, stretching anatomy," in *Proc. Hamlyn Symp. Med. Robotic*, 2018, pp. 103–104.

[10] E. Kucukdeger and B. N. Johnson, "Closed-loop controlled conformal 3D printing on moving objects via tool-localized object position sensing," *J. Manuf. Processes*, vol. 89, pp. 39–49, 2023.

[11] E. S. Barjuei, J. Shin, K. Kim, and J. Lee, "Precision improvement of robotic bioprinting via vision-based tool path compensation," *Sci. Reports*, vol. 14, no. 1, 2024, Art. no. 17764.

[12] Z. Zhang et al., "A multi-axis robot-based bioprinting system supporting natural cell function preservation and cardiac tissue fabrication," *Bioactive Materials*, vol. 18, pp. 138–150, 2022.

[13] D. Lee and A. Krupa, "Intensity-based visual servoing for non-rigid motion compensation of soft tissue structures due to physiological motion using 4D ultrasound," in *Proc. IEEE/RSJ Int. Conf. Intell. Robots Syst.*, 2011, pp. 2831–2836.

[14] R. Richa, A. P. L. Bó, and P. Poignet, "Towards robust 3D visual tracking for motion compensation in beating heart surgery," *Med. Image Anal.*, vol. 15, no. 3, pp. 302–315, 2011.

[15] L. Cuau, J. C. Santos, P. Poignet, and N. Zemiti, "Direct TPS-based 3D non-rigid motion estimation on 3D colored point cloud in eye-in-hand configuration," in *Proc. IEEE/RSJ Int. Conf. Intell. Robots Syst.*, 2024, pp. 11581–11586.

[16] M. Albouy et al., "A preliminary study for an intraoperative 3D bioprinting treatment of severe burn injuries," *Plast. Reconstructive Surg.– Glob. Open*, vol. 10, no. 1, 2022, Art. no. e4056.

[17] H. Ding and R. C. Chang, "Simulating image-guided in situ bioprinting of a skin graft onto a phantom burn wound bed," *Additive Manuf.*, vol. 22, pp. 708–719, 2018.